scientific reports

Check for updates

OPEN

Ferromagnetism modulation by ultralow current in a two-dimensional polycrystalline molybdenum disulphide atomic layered structure

Iriya Muneta[1]✉, Takanori Shirokura[2], Pham Nam Hai[2], Kuniyuki Kakushima[1], Kazuo Tsutsui[3] & Hitoshi Wakabayashi[1]

Layered materials, such as graphene and transition metal dichalcogenides, are able to obtain new properties and functions through the modification of their crystal arrangements. In particular, ferromagnetism in polycrystalline MoS_2 is of great interest because the corresponding nonmagnetic single crystals exhibit spontaneous spin splitting only through the formation of grain boundaries. However, no one has reported direct evidence of this unique phenomenon thus far. Herein, we demonstrate ferromagnetism modulation by an ultralow current density < 10^3 A/cm^2 in 7.5-nm-thick polycrystalline MoS_2, in which magnetoresistance shows three patterns according to the current intensity: wide dip, nondip and narrow dip structures. Since magnetoresistance occurs because of the interaction between the current of 4*d* electrons in the bulk and localized 4*d* spins in grain boundaries, this result provides evidence of the current modulation of ferromagnetism induced by grain boundaries. Our findings pave the way for the investigation of a novel method of magnetization switching with low power consumption for magnetic random access memories.

To develop spintronic devices and integrated circuits, such as magnetic random access memories, it is necessary to use current to generate an effective magnetic field for the manipulation of the individual magnetization in each element. To date, many investigations have given us clear evidence showing that electrical current can modulate the magnetization direction in magnetic tunnel junctions through spin transfer torque[1,2], spin–orbit torque[3], and the spin Hall effect in heavy 5*d* metal wires[4,5], which realizes magnetic random access memories with low energy consumption. However, magnetization manipulation still requires a large current density (> 10^5 A/cm^2). This is probably because typical ferromagnetic materials consist of 3*d* transition metals, in which intra- and interatomic exchange interactions of spins are too strong to interplay with electrical current.

The rearrangement of two-dimensional (2D) layered crystals is very important because novel properties and functions emerge that the bulk form of the corresponding material does not have. For example, bilayer graphene shows superconductivity[6] and Hofstadter's butterfly[7] by twisting the orientation of the upper layer; a 2D single-layer ferromagnet changes into an antiferromagnet by stacking one more layer[8]; and transition metal dichalcogenide MoS_2 shows memristive behaviour by connecting misoriented sheets that form grain boundaries (GBs)[9]. Moreover, MoS_2 is a not magnetic material in pure single-crystal form, but it has been found to show ferromagnetism in polycrystalline structures, edge-rich nanowires, and defective structures[10–19]. Additionally, theoretical analysis indicates that imperfections in MoS_2 crystals, such as point defects and topological defects, induce spin polarization in the 4*d* electrons of Mo atoms[20,21]. Since both conduction electrons and localized spins consist of mainly Mo 4*d* electrons, they would easily interact with each other because of the same orbital and relatively weaker intra- and interatomic exchange interactions in 4*d* spins compared to those of 3*d* ferromagnets. Thus, it can be estimated that magnetization will be easily modulated using electrical current in polycrystalline ferromagnetic MoS_2. In this study, we demonstrate the current-induced modulation of ferromagnetism in a

[1]Department of Electrical and Electronic Engineering, Tokyo Institute of Technology, Yokohama, Japan. [2]Department of Electrical and Electronic Engineering, Tokyo Institute of Technology, Tokyo, Japan. [3]Laboratory for Future Interdisciplinary Research of Science and Technology, Tokyo Institute of Technology, Yokohama, Japan. ✉email: muneta@ee.e.titech.ac.jp

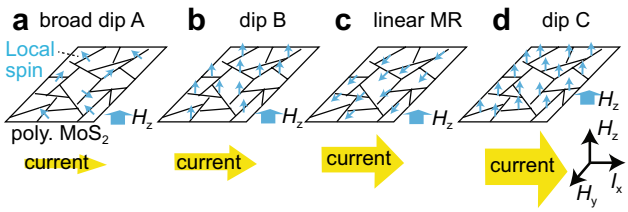

Figure 1. Schematic of the localized spin states in our magnetoresistance measurements. (**a**) In the small current applied, broad MR curves with dips A & A′ are observed in the H_z measurement because of the low spin density with disorder. (**b**) As the current increases, dip B with a large MR ratio is observed because of the high spin density along the H_z direction. (**c**) With a greater increase in current, the positive MR disappears, and flat or linear MR is observed because of the current-induced spin–orbit effective magnetic field along the H_y direction. (**d**) With a further increase in current, dip C is observed because of the high spin density, in which magnetization is along the H_z direction.

polycrystalline MoS_2 film with several nanometre grains[22,23] deposited by sputtering method, which produces a high density of GBs inducing ferromagnetism that we previously reported[11]. We measure the magnetic field H dependence of the magnetoresistance (MR) by applying a widely ranging current (1 nA–0.562 mA), by which we find that the MR curves show a variety of changes depending on the current intensity. Positive MR is mainly observed because of the spin-split band structure, and thus, we can estimate the magnetization properties, such as the coercive force, the magnetic field for magnetization saturation and the spin-split band structure inducing ferromagnetism. Additionally, linear MR is observed, which depends on the direction of the applied magnetic field.

Figure 1 shows a schematic representing the localized spin states in the H_z (out of plane) measurement. When the current is small, the spin density is not high enough to form magnetization in the whole film, so a magnetic field is needed to align the localized spins (Fig. 1a). As the current increases, current electrons start to be trapped at the GBs, which leads to an increase in the spin density and results in the spontaneous formation of film magnetization (Fig. 1b). As the current increases further, a current-induced magnetic field is effectively applied to the localized spins because of the spin-dependent scattering at the GBs, which results in the alignment of the localized spins along the H_y (in-plane) direction (Fig. 1c). With a further increase in current, the magnetization aligns along the H_z direction again because of a further increase in the localized spins in the GBs (Fig. 1d). The current density is estimated to be approximately 7×10^{-3} A/cm^2–4×10^3 A/cm^2 by dividing 1 nA–0.562 mA by the area defined by a 1.8 mm width and 7.5 nm depth. Considering the critical current of magnetization switching in magnetic tunnel junctions ($>10^5$ A/cm^2)[2,24–28], our MR modulation is successfully achieved at ultralow current densities ($<10^3$ A/cm^2), even though the spin–orbit interaction in 4*d* electrons is weaker than that in 5*d* electrons, which provides evidence that current electrons easily interact with the localized 4*d* spins in the GBs in a polycrystalline MoS_2 film. Our results place focus on the future investigation of 4*d* ferromagnets[29], polycrystalline ferromagnetic semiconductors, and recently discovered 2D ferromagnets[8,30–34], by controlling and manipulating ferromagnetism via basic electronics with low power consumption[35–39].

Results and discussion

In our previous study, out-of-plane 2θ–θ X-ray diffraction was measured[40], in which MoS_2 (002) peak was observed at $2\theta = 13.5°$. Using Bragg's law, we can estimate the layer distance of MoS_2 $c = n\times\lambda/2\sin\theta = 6.56$ Å. Here, we use $n = 1$ and $\lambda = 1.5418$ Å (wavelength of Cu$K\alpha$). It is confirmed that this value is near the layer distance of bulk MoS_2 ($c = 6.15$ Å)[41]. The observed MoS_2 (002) peak is broad because our sample is polycrystal with imperfection of periodicity and incomplete flatness of van deer Waals surface.

Also, in our previous study, height distribution of MoS_2 surface fabricated by sputter in the similar condition was measured using atomic force microscopy, in which root mean square (RMS) was 0.515 nm[42]. Compared to monolayer MoS_2 by the chemical vaper deposition, this value is not bad because it is less than two layers distance 0.656 nm. Thus, our polycrystal MoS_2 keeps van der Waals horizontal structure.

In addition, cross sectional lattice structure in polycrystal MoS_2 was observed using the transmission electron microscopy (TEM) in our previous study[11], from which we guess that the grain size is 5 nm. Based on this value, we can estimate the ratio of Mo atoms along GBs as follows. We assume x cm $\times$ y cm polycrystal monolayer MoS_2, in which grains are regular squares with 5 nm edge length and are arranged like the grid of a checkerboard. The length of GBs is x cm/5 nm $\times$ y cm $\times$ 2 = $4xy\times10^6$ cm, while the Mo density in GBs is 1/3.16 Å = $1/3.16\times10^8$ cm^{-1}, in which we assume that Mo-Mo distance in GBs is 3.16 Å. Thus, the number of Mo atoms along GBs is $1/3.16\times10^8$ cm$^{-1}\times4xy\times10^6$ cm = $xy\times1.27\times10^{14}$ atoms. In single crystal monolayer MoS_2 with $a = 3.16$ Å[41], the Mo density is 1.16×10^{15} cm^{-2}, and thus, the number of Mo atoms in the bulk area of xy cm^2 is $xy\times1.16\times10^{15}$ atoms. Therefore, the ratio of Mo atoms along GBs and in bulk is $(xy\times1.27\times10^{14})/(xy\times1.16\times10^{15}) = 11\%$. This result agrees with the density of magnetic Mo atoms 0.61–16% estimated from the saturation magnetization 1–26 emu/cm^3 reported in our previous study (see "Calculation for the density of magnetic Mo atoms" in "Methods" section)[11].

Moreover, TEM image in Ref.[11] provides us information about surface morphology: The most surface layer is incontiguous and interrupts by several nm. This surface morphology agrees with RMS value 0.515 nm from the AFM measurement[42]. See Supplementary Fig. 1 for the Raman measurement, the temperature dependence of resistance and the voltage-current characteristic.

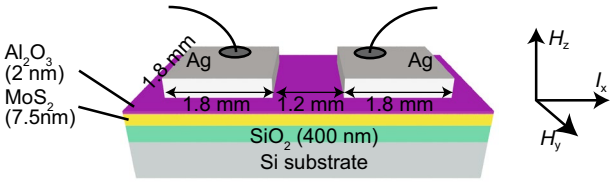

Figure 2. Schematic sample structure examined in our magnetoresistance measurement. Current is applied along the I_x direction between the two Ag contacts formed at the surface. The in-plane (out-of-plane) magnetic field is applied along the H_y (H_z) direction.

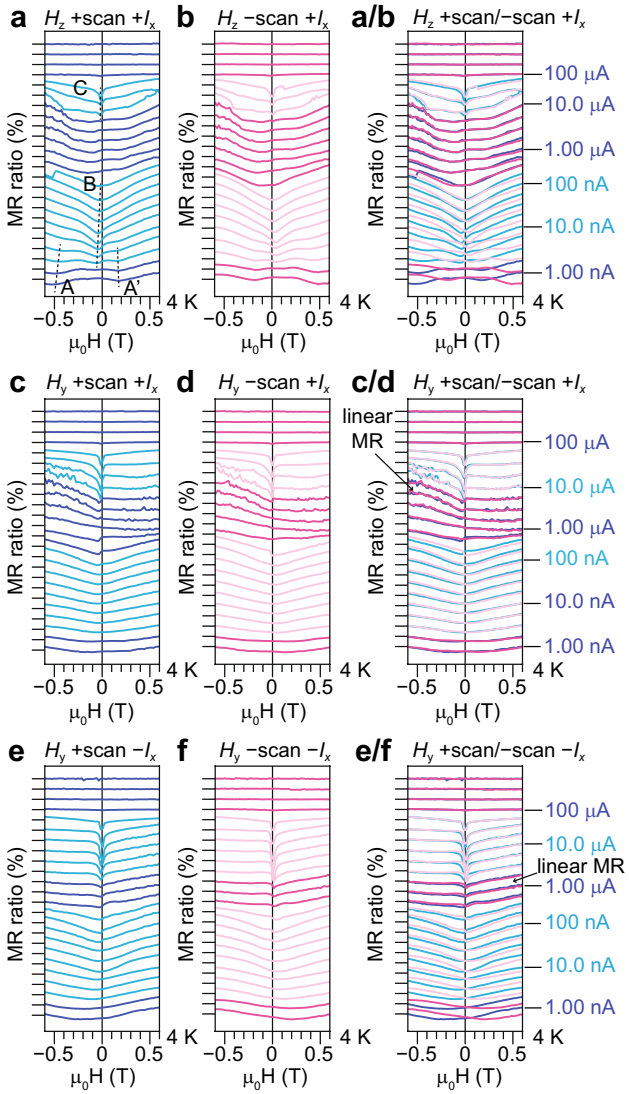

Figure 3. Magnetoresistance measured with various current intensities at 4 K. The current increases in steps of 1.78 times. (**a**,**b**) Magnetic field is applied along the out-of-plane direction (H_z). (**c**–**f**) Magnetic field is applied along the in-plane direction crossing the current (H_y). The current directions are + I_x (**a**–**d**) and − I_x (**e**,**f**). The magnetic field is swept from positive to negative (+ scan) in (**a**,**c**,**e**) and from negative to positive (− scan) in (**b**,**d**,**f**). (**a**/**b**,**c**/**d**,**e**/**f**) are superimposed together with + scan and − scan curves. The tick on the left axis indicates 0 in each curve. The tick space indicates 2%.

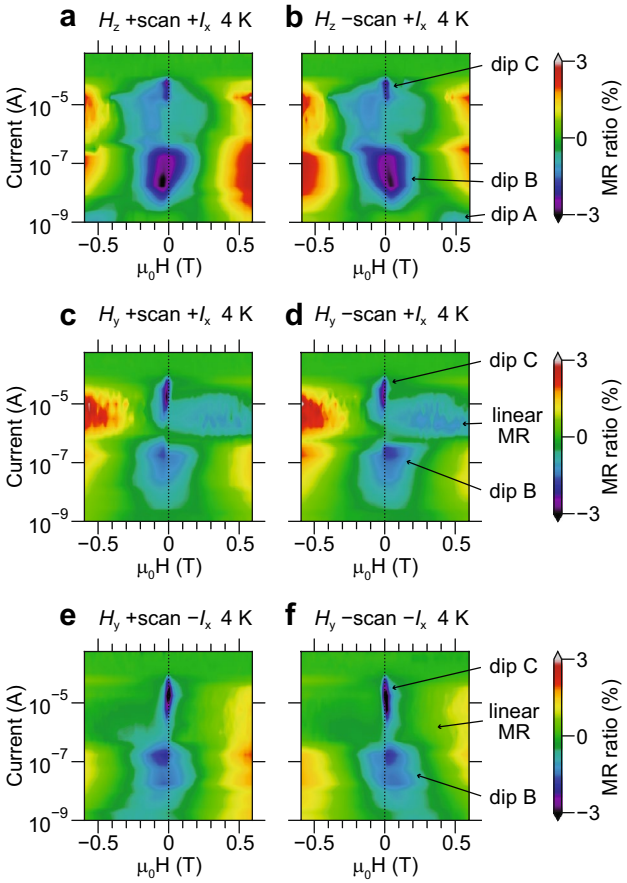

Figure 4. Colour-coded map of magnetoresistance measured with various currents at 4 K. (**a**,**b**) Magnetoresistance as functions of current and magnetic field applied along the out-of-plane direction (H_z). (**c**–**f**) Magnetoresistance as functions of current and magnetic field applied along the in-plane direction crossing the current (H_y). The current directions are $+I_x$ (**a**–**d**) and $-I_x$ (**e**,**f**). The magnetic field is swept from positive to negative (+scan) (**a**,**c**,**d**) and from negative to positive (−scan) (**b**,**d**,**f**).

We analyse the details of the MR data measured in the two terminal device shown in Fig. 2. The MR-H curves measured at various currents are shown as multiple-curve plots in Fig. 3, where these curves are summarized according to the directions of H and the current. These curves are transformed into the colour-coded maps shown in Fig. 4. The MR-H curves mainly show positive MR curves, and a linear MR feature is observed in the H_y measurement. The positive MR curves are divided into three types: dips A and A′ with a large offset of H, dip B with a wide shape and dip C with a sharp shape. These observations indicate that the ferromagnetism in polycrystalline MoS_2 is modulated by the applied current.

From the measurement data, we extract the physical values: the dip gap between + scan and -scan for dips B and C, $MR_{max} - MR_{min}$, the c and d values of dips B and C obtained by fitting to the Khosla–Fischer equation[43], and the slope of the odd function as a function of current, as shown in Fig. 5 (see "Methods" section for detail). The Khosla–Fischer equation represents positive MR based on up- and down-spin band model[43], in which the parameters c and d are described by mobility and conductivity of up- and down-spin bands[44–47]. According to Takiguchi et al., conductivity can be described by the band energy, and thus, the spin split energy can be obtained from the d value by using this semi-empirical model (see "Calculation for spin split energy" in "Methods" section)[48]. Also, magnetic field for the saturation magnetization H_s can be evaluated numerically, so we can analyze it as a function of the current intensity.

As shown in Fig. 5a,f,k, the dip gap between + scan and − scan, which corresponds to coercive force H_c, decreases 1/30 times as the current increases. A similar behaviour is seen in $Ga_{1-x}Mn_xAs$, where the coercive force significantly decreases as the magnetic impurity x increases[49]. Based on this analogy, we can suppose that the density of spin magnetic moments increases as the current increases in polycrystalline MoS_2.

As shown in Fig. 5d,i,n, the d value, which corresponds to the dip width and correlates to H_s, is 20 times larger for dip C than for dip B. This behaviour is also seen in the $Ga_{1-x}Mn_xAs$ case reported in Ref.[49], where H_s decreases as x increases. The dip gap and d value data indicate that the ferromagnetic properties are changed only by increasing the current without changing the magnetic doping required in typical ferromagnetic semiconductors.

The magnetic properties H_c and H_s are influenced by the density of magnetic atoms or distance between neighboring spins. Thus, similar density is one of the reasons of comparable behaviour of H_c and H_s in these two

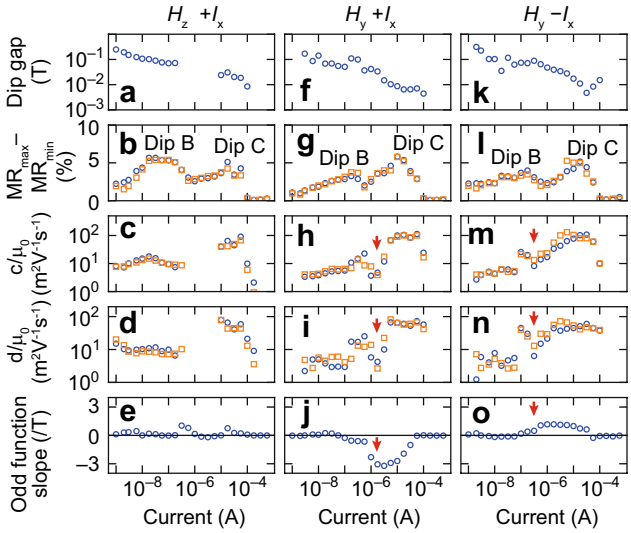

Figure 5. Dip gap, MR ratio, c value, d value and odd function slope obtained from our magnetoresistance measurements. (**a**–**e**) Data obtained in $H_z + I_x$ measurement. (**f**–**j**) Data obtained in $H_y + I_x$ measurement. (**k**–**o**) Data obtained in $H_y - I_x$ measurement. Blue circles and orange squares in (**b**–**d**,**g**–**i**,**l**–**o**) correspond to + scan and − scan, respectively.

materials. The density of magnetic atoms of GaMnAs in Ref.[49] is 0.5% and 7.4%. Meanwhile, the density of the magnetic atoms in our polycrystal MoS_2 is estimated to be 0.61–16% using saturation magnetization 1–26 emu/cm^3 measured on polycrystal MoS_2 fabricated in the similar condition in our previous study (see "Calculation for the density of magnetic Mo atoms" in "Methods" section)[11]. Additionally, the similar mechanism of ferromagnetism in these two materials supports the comparison of the descriptions of H_c and H_s. The mechanism of ferromagnetism in GaMnAs is carrier mediated exchange interaction between 3*d* localized spins, while the presumed mechanism of ferromagnetism in polycrystal MoS_2 is carrier assisted exchange interaction between 4*d* localized spins in GBs. It is noted that H_c decreases has been observed in InMnAs as the increase in MnAs fraction[50].

Additionally, we can estimate the spin-split energy of the 4*d* band from the d values[44,48], which are 2.5 meV and 100 meV for dips B and C, respectively (see "Calculation for spin split energy" in "Methods" section for details). Although this estimation includes many assumptions, the derived values are worth considering for the band structure of polycrystalline MoS_2 because the order of these values is near that of the theoretical calculation[20,21].

The ferromagnetism enhancement by current probably occurs because the charges are trapped at the spin-dependent 4*d* sites in the Mo atoms in the GBs or because the itinerant carrier density increases in the long channel.

Linear MR starts to be observed at 3.9 A/cm^2 (0.56 μA) (see in Fig. 3c/d,e/f to check which curves are linear MR). If the efficiency of the equivalent field because of the spin–orbit torque is the same as GaMnAs [99 Oe/(1 MA/cm^2)][3], the effective magnetic field at 3.9 A/cm^2 is 0.39 mOe. This value is quite small to change magnetic behaviour in the sample, and thus, the mechanism of MR change is thought to be different from the spin–orbit torque observed in 3*d* metal ferromagnets and ferromagnetic semiconductors. Conceivable mechanism of linear MR is the change of occupancy in 4*d* orbitals of Mo atoms in GBs because of spin-dependent scattering and the change of electron density in the long channel. The change of occupancy results in the change of the exchange interaction between localized 4*d* spins and results in the change of magnetic anisotropy because of spin–orbit interaction between spins and 4*d* orbitals with the magnetic quantum number.

In Ref.[51], linear MR was observed in $SmCo_5$ when the magnetization was independent of the magnetic field. This is described by Equation $\boldsymbol{j} = A(\boldsymbol{M}\cdot\boldsymbol{H})\boldsymbol{E}$ with steady $\boldsymbol{M}$ when $\boldsymbol{H}$ is swept, where $\boldsymbol{j}$, A, $\boldsymbol{M}$ and $\boldsymbol{E}$ are the current vector, coefficient, magnetization vector and electric field vector, respectively. As far as this theory is concerned, our observation of linear MR in the H_y measurement indicates that $\boldsymbol{M}$ is fixed to in-plane directions because of the spin–orbit effective magnetic field and the change of the exchange interaction induced by the current (Fig. 1c). This hypothesis is confirmed by the three pieces of experimental evidence below. One: When flipping the current direction, the odd function shows the opposite sign of slope (see Fig. 5j,o and "Calculation for linear MR" in "Methods" section). This is thought to occur because flipping the current leads to flipping the direction of the spin–orbit effective magnetic field, and thus, the sign of $\boldsymbol{M}$ flips. Two: There is no hysteresis. A similar shape of MR is observed between + scan and − scan. From this, we can guess that the localized spins are not ordered by the external magnetic field, but their directions are determined by spin–orbit effective magnetic field through the current. Three: In the H_z measurement, flat MR is observed when H_z is small (from − 0.3 to + 0.3 T) in the current region where linear MR is observed in the H_y measurement (Fig. 5e,j,o). This is because $\boldsymbol{M}$ is oriented in the in-plane direction, but $\boldsymbol{H}$ is out of plane; thus, $\boldsymbol{M}\cdot\boldsymbol{H} = 0$. Moreover, when a large magnetic field is applied,

$\boldsymbol{M}$ is released from the domination by current and is oriented to H_z, and thus, the MR curve shows a kink (see MR data at 10 μA in Supplementary Fig. 2).

For the H_y measurements, linear MR starts to be observed when the positive MR starts to weaken (indicated by arrows in Fig. 5h–j,m–o). This indicates that the current-induced spin–orbit effective magnetic field changes the exchange interaction between the localized spins.

Double dips are seen for low current denoted by dips A and A′ (Fig. 3a,b). The reason for this is speculated to be that the magnetic domain is not single-domain but is multidomain, or likely because the magnetization direction is variously changed.

The disappearance of MR above 0.1 mA is probably because the localized 4*d* levels are fully occupied or because spin-dependent scattering does not occur because of the high current intensity.

Our results are related to recent progress of 2D ferromagnets, recommend 4*d* transition metal compounds as materials for spintronics, and indicate that the arrangement of polycrystalline structures unveils hidden characteristics and phenomena related to the interactions between localized spins and itinerant electrons.

Methods

Fabrication. We deposited a polycrystalline MoS_2 film (7.5 nm) on a SiO_2 (400 nm)/Si (0.7 mm) substrate using radio-frequency (RF) magnetron sputtering (EIKO ENGINEERING, LTD.) with a 4 N-purity MoS_2 target (Matsurf Technologies Inc.). The sputtering conditions were as follows: the substrate temperature was 450 °C, Ar pressure was 0.35 Pa with 7 sccm flow, the substrate-target distance was 180 mm, and the RF power was 40 W. After deposition, we deposited an Al_2O_3 layer (2 nm) on the sample using atomic layer deposition (Fiji Inc.) at 300 °C with $(CH_3)_3Al$ (trimethylaluminium; TMA) and H_2O as precursors. Next, we deposited Ag pads (50 nm thickness) as electrical contacts using a current-heating vacuum evaporation tool with a shadow mask placed in front of the sample. The Ag pad pattern was a 1.8 mm × 1.8 mm square array with a 1.2 mm space. Finally, we cut the sample into small specimens, including 2 Ag pads, and bonded Au wires on them to connect to the electrodes in a sample holder.

Magnetoresistance measurement. We performed magnetoresistance measurements using our custom-made 4 K cryostat equipment and Keithley 2400 as a source measure unit. The magnetic field was first applied at + 0.8 T and swept towards − 0.8 T at a 20 mT step (+ scan). After that, the field was swept from − 0.8 to + 0.8 T (− scan). Each magnetoresistance curve was normalized by dividing by the average value of the curve $(R - R_{ave})/R_{ave} \times 100$.

Data analysis. To extract physical values from MR curves, we used the following equation for positive MR:

$$\frac{R - R_{AVE}}{R_{AVE}}(\%) = \sum_i \frac{c_i^2 \left(H - H_0^i\right)^2}{1 + d_i^2 \left(H - H_0^i\right)^2}, \tag{1}$$

where H_0 is the centre position of positive MR. The summation of multiple curves was performed because the curve structure was not simple, but we discussed only the parameters for dips B and C. The fitting results and each component of the curves are shown in Supplementary Figs. 2–7.

Calculation for spin split energy. We estimated the spin-split energy of the 4*d* band from the d values by using equation[44,48],

$$d^2 = \frac{(\sigma_1\mu_2 - \sigma_2\mu_1)^2}{(\sigma_1 + \sigma_2)^2},$$

in which subscripts 1 and 2 represent up and down spins, respectively. In 2D system, the band energy is described by electron density,

$$E_i = \frac{2\pi\hbar^2}{m^*} n_i (i = 1, 2),$$

where μ, n, ħ, m^* correspond to the mobility, two-dimensional electron density, plank constant, and effective mass of electron, respectively. The relation between conductivity and electron density is

$$\sigma_i = q n_i \mu_i, (i = 1, 2).$$

Thus, d value can be modified using above equations,

$$d = \frac{1}{\frac{n_1}{\mu_2} + \frac{n_2}{\mu_1}}(n_1 - n_2) = \frac{1}{\frac{n_1}{\mu_2} + \frac{n_2}{\mu_1}} \frac{m^*}{2\pi\hbar^2}\Delta E \approx \frac{\mu}{n}\frac{m^*}{2\pi\hbar^2}\Delta E, \tag{2}$$

where ΔE represents spin split energy of the 4*d* band. With the assumption of $\mu = 0.01\ cm^2/V/s$, $n = 10^{11}/cm^2$ for dip B, $n = 2 \times 10^{11}/cm^2$ for dip C and $m^* = m_0$ (electron mass), ΔE is estimated to be 2.5 meV and 100 meV for dips B ($d/\mu_0 = 4\ m^2/V/s$) and C ($d/\mu_0 = 80\ m^2/V/s$), respectively. Here, μ_0 is the vacuum permeability.

Calculation for linear MR. To clearly observe linear MR, we examined odd functions by using $[MR_+(H) - MR_-(-H)]/2$, where MR_+ and MR_- correspond to the MR observed in the + scan and − scan meas-

urements, respectively. The extracted odd function data are shown in Supplementary Figs. 8–10. The slope of odd function was numerically obtained by fitting the odd functions to a linear equation $y = ax + b$. The obtained values are shown in Fig. 5e,j,o.

Calculation for the density of magnetic Mo atoms. Since there are $1 + 6/3 = 3$ Mo atoms in a regular hexagon with one side length $a = 3.16$ Å, we calculated the number of Mo atoms in a square centimeter in monolayer MoS_2:

$$\frac{3}{\frac{3\sqrt{3}}{2}a^2} = 1.156 \times 10^{15}\,\mathrm{cm}^{-2}.$$

Similarly, the number of Mo atoms in a centimeter along out-of-plane direction was calculated:

$$\frac{1}{6.55\,\text{Å}} = 1.527 \times 10^{7}\,\mathrm{cm}^{-1}.$$

Thus, the density of Mo atoms in multilayer MoS_2 was calculated:

$$1.156 \times 10^{15}\,\mathrm{cm}^{-2} \times 1.527 \times 10^{7}\,\mathrm{cm}^{-1} = 1.765 \times 10^{22}\,\mathrm{Mo/cm}^{3}. \quad (3)$$

The saturation magnetization in Ref.[11] was described using Bohr magneton μ_B:

$$1\,\mathrm{emu/cm}^{3} = 1.078 \times 10^{20}\,\mu_B/\mathrm{cm}^{3}. \quad (4)$$

This means the number of spin 1/2 in a cubic centimeter. The density of magnetic Mo atoms was calculated by dividing Eq. (4) with Eq. (3):

$$\frac{1.078 \times 10^{20}\,\mu_B/\mathrm{cm}^{3}}{1.765 \times 10^{22}\,\mathrm{Mo/cm}^{3}} = 0.611 \times 10^{-2}\,\mu_B/\mathrm{Mo}.$$

This means that 0.61% of Mo atoms have one spin 1/2.

Data availability

All data generated during this study are included in Supplementary Information files.

Received: 27 June 2022; Accepted: 10 October 2022
Published online: 13 October 2022

References

1. Ikeda, S. *et al.* Magnetic tunnel junctions for spintronic memories and beyond. *IEEE Trans. Electron Devices* **54**, 991–1002 (2007).
2. Chiba, D., Sato, Y., Kita, T., Matsukura, F. & Ohno, H. Current-driven magnetization reversal in a ferromagnetic semiconductor (Ga, Mn)As/GaAs/(Ga, Mn)As tunnel junction. *Phys. Rev. Lett.* **93**, 216602 (2004).
3. Jiang, M. *et al.* Efficient full spin-orbit torque switching in a single layer of a perpendicularly magnetized single-crystalline ferromagnet. *Nat. Commun.* **10**, 2590 (2019).
4. Conte, R. L. *et al.* Spin-orbit torque-driven magnetization switching and thermal effects studied in Ta/CoFeB/MgO nanowires. *Appl. Phys. Lett.* **105**, 122404 (2014).
5. Hao, Q. & Xiao, G. Giant spin Hall effect and switching induced by spin-transfer torque in a $W/Co_{40}Fe_{40}B_{20}/MgO$ structure with perpendicular magnetic anisotropy. *Phys. Rev. Appl.* **3**, 034009 (2015).
6. Cao, Y. *et al.* Unconventional superconductivity in magic-angle graphene superlattices. *Nature* **556**, 43–50 (2018).
7. Dean, C. R. *et al.* Hofstadter's butterfly and the fractal quantum Hall effect in moiré superlattices. *Nature* **497**, 598–602 (2013).
8. Huang, B. *et al.* Layer-dependent ferromagnetism in a van der Waals crystal down to the monolayer limit. *Nature* **546**, 270–273 (2017).
9. Sangwan, V. K. *et al.* Gate-tunable memristive phenomena mediated by grain boundaries in single-layer MoS_2. *Nat. Nanotechnol.* **10**, 403–406 (2015).
10. Zhang, J. *et al.* Magnetic molybdenum disulfide nanosheet films. *Nano Lett.* **7**, 2370–2376 (2007).
11. Shirokura, T., Muneta, I., Kakushima, K., Tsutsui, K. & Wakabayashi, H. Strong edge-induced ferromagnetism in sputtered MoS_2 film treated by post-annealing. *Appl. Phys. Lett.* **115**, 192404 (2019).
12. Mathew, S. *et al.* Magnetism in MoS_2 induced by proton irradiation. *Appl. Phys. Lett.* **101**, 102103 (2012).
13. Tongay, S., Varnoosfaderani, S. S., Appleton, B. R., Wu, J. & Hebard, A. F. Magnetic properties of MoS_2: Existence of ferromagnetism. *Appl. Phys. Lett.* **101**, 123105 (2012).
14. Zhang, R., Li, Y., Qi, J. & Gao, D. Ferromagnetism in ultrathin MoS_2 nanosheets: From amorphous to crystalline. *Nanoscale Res. Lett.* **9**, 586 (2014).
15. Sun, B., Li, Q. L. & Chen, P. Room-temperature ferromagnetism of single-crystalline MoS_2 nanowires. *Micro Nano Lett.* **9**, 468–470 (2014).
16. Xu, G. *et al.* Metallic and ferromagnetic MoS_2 nanobelts with vertically aligned edges. *Nano Res.* **8**, 2946–2953 (2015).
17. Kondo, G. *et al.* Edge-spin-derived magnetism in few-layer MoS_2 nanomeshes. *AIP Adv.* **7**, 125019 (2017).
18. Gao, G. *et al.* Toward edges-rich MoS_2 layers via chemical liquid exfoliation triggering distinctive magnetism. *Mater. Res. Lett.* **5**, 267–275 (2017).
19. Zhou, Q. *et al.* Robust ferromagnetism in zigzag-edge rich MoS_2 pyramids. *Nanoscale* **10**, 11578–11584 (2018).
20. Zhang, Z., Zou, X., Crespi, V. H. & Yakobson, B. I. Intrinsic magnetism of grain boundaries in two-dimensional metal dichalcogenides. *ACS Nano* **7**, 10475–10481 (2013).
21. Gao, N., Guo, Y., Zhou, S., Bai, Y. & Zhao, J. Structures and magnetic properties of MoS_2 grain boundaries with antisite defects. *J. Phys. Chem. C* **121**, 12261–12269 (2017).
22. Ohashi, T. *et al.* Multi-layered MoS_2 film formed by high-temperature sputtering for enhancement-mode nMOSFETs. *Jpn. J. Appl. Phys.* **54**, 04DN08 (2015).

23. Ishihara, S. *et al.* Improving crystalline quality of sputtering-deposited MoS_2 thin film by postdeposition sulfurization annealing using $(t\text{-}C_4H_9)_2S_2$. *Jpn. J. Appl. Phys.* **55**, 04EJ07 (2016).
24. Mangin, S. *et al.* Current-induced magnetization reversal in nanopillars with perpendicular anisotropy. *Nat. Mater.* **5**, 210–215 (2006).
25. Ikeda, S. *et al.* A perpendicular-anisotropy CoFeB–MgO magnetic tunnel junction. *Nat. Mater.* **9**, 721–724 (2010).
26. Chen, E. *et al.* Advances and future prospects of spin-transfer torque random access memory. *IEEE Trans. Magn.* **46**, 1873–1878 (2010).
27. Liu, L., Lee, O. J., Gudmundsen, T. J., Ralph, D. C. & Buhrman, R. A. Current-induced switching of perpendicularly magnetized magnetic layers using spin torque from the spin Hall effect. *Phys. Rev. Lett.* **109**, 096602 (2012).
28. Thomas, L. *et al.* Perpendicular spin transfer torque magnetic random access memories with high spin torque efficiency and thermal stability for embedded applications (invited). *J. Appl. Phys.* **115**, 172615 (2014).
29. Wakabayashi, Y. K. *et al.* Single-domain perpendicular magnetization induced by the coherent O 2*p*-Ru 4*d* hybridized state in an ultra-high-quality $SrRuO_3$ film. *Phys. Rev. Mater.* **5**, 124403 (2021).
30. Gong, C. *et al.* Discovery of intrinsic ferromagnetism in two-dimensional van der Waals crystals. *Nature* **546**, 265–269 (2017).
31. Wang, Z. *et al.* Electric-field control of magnetism in a few-layered van der Waals ferromagnetic semiconductor. *Nat. Nanotechnol.* **13**, 554–559 (2018).
32. Bonilla, M. *et al.* Strong room temperature ferromagnetism in VSe_2 monolayers on van der Waals substrates. *Nat. Nanotechnol.* **13**, 289–293 (2018).
33. Avsar, A. *et al.* Defect induced layer-modulated magnetism in ultrathin metallic $PtSe_2$. *Nat. Nanotechnol.* **14**, 674–678 (2019).
34. O'Hara, D. J. *et al.* Room temperature intrinsic ferromagnetism in epitaxial manganese selenide films in the monolayer limit. *Nano Lett.* **18**, 3125–3131 (2018).
35. Gupta, V. *et al.* Manipulation of the van der Waals magnet $Cr_2Ge_2Te_6$ by spin-orbit torques. *Nano Lett.* **20**, 7482–7488 (2020).
36. Wang, X. *et al.* Current-driven magnetization switching in a van der Waals ferromagnet Fe_3GeTe_2. *Sci. Adv.* **5**, eaaw8904 (2019).
37. Alghamdi, M. *et al.* Highly efficient spin-orbit torque and switching of layered ferromagnet Fe_3GeTe_2. *Nano Lett.* **19**, 4400–4405 (2019).
38. Xu, Y. *et al.* Coexisting ferromagnetic-antiferromagnetic state in twisted bilayer CrI_3. *Nat. Nanotechnol.* **17**, 143–147 (2022).
39. Telford, E. J. *et al.* Coupling between magnetic order and charge transport in a two-dimensional magnetic semiconductor. *Nat. Mater.* **21**, 754–760 (2022).
40. Imai, S. *et al.* Importance of crystallinity improvement in MoS_2 film by compound sputtering even followed by post sulfurization. *Jpn. J. Appl. Phys.* **60**, SBBH10 (2021).
41. Wildervanck, J. C. & Jellinek, F. Preparation and crystallinity of molybdenum and tungsten sulfides. *Z. Anorg. Allg. Chem.* **328**, 309–318 (1964).
42. Ohashi, T. *et al.* Quantitative relationship between sputter-deposited-MoS_2 properties and underlying-SiO_2 surface roughness. *Appl. Phys. Expr.* **10**, 041202 (2017).
43. Khosla, R. P. & Fischer, J. R. Magnetoresistance in degenerate CdS: Localized magnetic moments. *Phys. Rev. B* **2**, 4084–4097 (1970).
44. Peters, J. A., Parashar, N. D., Rangaraju, N. & Wessels, B. W. Magnetotransport properties of InMnSb magnetic semiconductor thin films. *Phys. Rev. B* **82**, 205207 (2010).
45. Tu, N. T., Hai, P. N., Anh, L. D. & Tanaka, M. Magnetic properties and intrinsic ferromagnetism in (Ga, Fe)Sb ferromagnetic semiconductors. *Phys. Rev. B* **92**, 144403 (2015).
46. Venkatesh, S. *et al.* Defect-band mediated ferromagnetism in Gd-doped ZnO thin films. *J. Appl. Phys.* **117**, 013913 (2015).
47. An, Y., Ren, Y., Yang, D., Wu, Z. & Liu, J. Oxygen vacancy-induced room temperature ferromagnetism and magnetoresistance in Fe-doped In_2O_3 films. *J. Phys. Chem. C* **119**, 4414–4421 (2015).
48. Takiguchi, K. *et al.* Giant gate-controlled proximity magnetoresistance in semiconductor-based ferromagnetic–non-magnetic bilayers. *Nat. Phys.* **15**, 1134–1139 (2019).
49. Hayashi, T., Tanaka, M., Nishinaga, T. & Shimada, H. Magnetic and magnetotransport properties of new III–V diluted magnetic semiconductors: GaMnAs. *J. Appl. Phys.* **81**, 4865–4867 (1997).
50. Novák, J., Dujavová, A., Vávra, I., Hasenöhrl, S. & Reiffers, M. Magnetic properties of InMnAs nanodots prepared by MOVPE. *J. Magn. Magn. Mater.* **327**, 20–23 (2013).
51. Wang, Y. *et al.* Antisymmetric linear magnetoresistance and the planar Hall effect. *Nat. Commun.* **11**, 216 (2020).

Acknowledgements

This work was supported by Grants-in-Aid for Early-Career Scientists (18K13785 and 21K14193) by Japan Society for the Promotion of Science, Iketani Science and Technology Foundation (0311055-A) and Mizuho Foundation for the Promotion of Sciences (KJ20050048).

Author contributions

I.M. planned this research, found the current dependence of the magnetoresistance, synthesized the experiment and analysed the total data. T.S. developed the initial magnetoresistance experiment. P.N.H. and K.K. advised on the experiment. I.M., P.N.H., K.T. and H.W. wrote the manuscript and supervised the publication of this work.

Competing interests

The authors declare no competing interests.

Additional information

Supplementary Information The online version contains supplementary material available at https://doi.org/10.1038/s41598-022-22113-3.

Correspondence and requests for materials should be addressed to I.M.

Reprints and permissions information is available at www.nature.com/reprints.

Publisher's note Springer Nature remains neutral with regard to jurisdictional claims in published maps and institutional affiliations.